ATLAS CONF Note

ATLAS-CONF-2024-011

July 23, 2024

Search for displaced leptons in 13 TeV and 13.6 TeV pp collisions with the ATLAS detector

The ATLAS Collaboration

A search for leptons, displaced from the primary interaction vertex, including data collected at a center-of-mass energy of 13.6 TeV by the ATLAS experiment during Run 3 of the Large Hadron Collider is presented. The data sample used includes the full LHC Run 2 dataset of $\sqrt{s}$ = 13 TeV proton–proton collisions with an integrated luminosity of 140 fb^{-1}, and the partial $\sqrt{s}$ = 13.6 TeV Run 3 dataset collected in 2022–2023 corresponding to an integrated luminosity of 56.3 fb^{-1}. Final states with displaced electrons and/or muons are considered, and novel triggers introduced in Run 3 are employed that use large radius tracking to reconstruct displaced tracks with low momentum. In addition, photon reconstruction and multivariate techniques are employed to broaden sensitivity to channels with large background rates or highly displaced electrons, respectively. The results are consistent with the Standard Model background expectations and are used to set model-independent limits on the production of displaced electrons and muons. The analysis is also interpreted in the context of a gauge-mediated supersymmetry breaking model with pair-produced long-lived sleptons. The results include 95% CL exclusions of selectrons of 150 GeV mass with lifetime values from 4 ps to 70 ns, and of selectrons, smuons and staus with 0.3 ns lifetime up to masses of 740 GeV, 840 GeV, and 380 GeV, respectively.

1 Introduction

Long-lived particles (LLPs) occur in the Standard Model (SM), and are predicted in a wide variety of beyond-the-SM (BSM) scenarios, including both R-parity-conserving [1–7] and R-parity-violating supersymmetry (SUSY) [8, 9], split-SUSY [10, 11], gauge-mediated SUSY breaking (GMSB) [12–14], universal extra dimensions [15, 16], and Hidden Valley models [17]. Most searches for beyond-the-SM (BSM) physics at the Large Hadron Collider (LHC) experiments assume that BSM particles decay promptly, producing final state particles with trajectories consistent with an origin at the primary proton-proton (pp) interaction point. By contrast, LLPs with lifetimes longer than a few picoseconds travel at least hundreds of microns before decaying. Their decay products can thus be displaced from the primary vertex (PV), the vertex with the largest sum of squared track transverse momentum, or delayed with respect to the bunch crossing. Reconstruction of the decay products can pose technical challenges that could have caused them to elude detection in prior searches.

This paper presents a search for BSM physics in events with two displaced light leptons (electrons or muons). The search is performed with inclusive selection criteria to enable broad sensitivity to BSM models producing LLPs, with lifetimes from a few ps up to of order 100 ns, that decay to electrons or muons. As a benchmark model, the sensitivity of the search is illustrated using a GMSB SUSY model [18–20] in which the lightest SUSY particle (LSP) is a nearly massless gravitino ($\tilde{G}$) and the next-to-lightest SUSY particle (NLSP) is a slepton ($\tilde{\ell}$), which can be either a selectron ($\tilde{e}$), smuon ($\tilde{\mu}$), or stau ($\tilde{\tau}$). As shown in Figure 1, the NLSP can be pair-produced, and then each decays to a charged SM lepton (ℓ) of the same flavor and a gravitino LSP, yielding events containing two displaced leptons. The slepton can acquire a long lifetime due to its small gravitational coupling to the gravitino LSP. GMSB models often predict that staus are the NLSP [21].
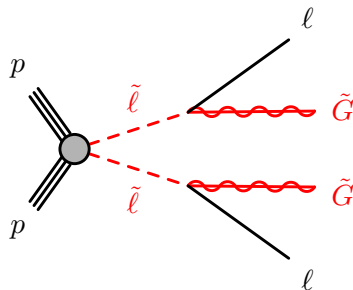

Figure 1: Diagram depicting the GMSB slepton model.

Previous results setting limits on these processes include an ATLAS search using the full Run 2 dataset, consisting of 140 fb^{-1} of pp collisions collected at $\sqrt{s}$ = 13 TeV, which excluded selectrons, smuons, and staus with masses up to 720 GeV, 680 GeV, and 340 GeV, respectively, for a slepton lifetime of 0.1 ns [22], dramatically enhancing the sensitivity with respect to prior constraints from the LEP experiments [23–27]. A CMS search based on 113–118 fb^{-1} of 13 TeV pp collisions extended the stau mass reach to 405 GeV for similar lifetime [28]. A subsequent full Run 2 ATLAS search for muons with intermediate displacements, in between those of the displaced and prompt lepton searches, extended the sensitivity to GMSB smuons with lifetimes below about 0.01 ns [29].

This result enhances the discovery reach for displaced leptons beyond that of prior searches through several novel additions. It includes data collected by the ATLAS detector at a center-of-mass energy of 13.6 TeV, new triggers introduced in Run 3 that exploit improved tracking capabilities of the high-level trigger

(HLT) to enable lower lepton transverse momentum (p_T) thresholds, as well as improved offline tracking performance that greatly lowers the rate of incorrectly reconstructed displaced tracks [30]. Precision information from the ATLAS Liquid Argon (LAr) electromagnetic (EM) calorimeter is introduced for sensitivity to highly displaced electrons, which may fail to include reconstructed tracks and be reconstructed as photons. Finally, the analysis includes a first consideration of single displaced electron channels, which were previously inaccessible due to high background rates and are enabled using multivariate Boosted Decision Trees (BDTs).

The analysis combines two approaches with mutually exclusive selections. In both cases, backgrounds are determined with entirely data-driven methods, and Monte Carlo (MC) simulation is only used for signal models. The "ABCD" search targets dilepton events, requiring at least two electrons, two muons, or an electron and a muon, and uses similar techniques as the prior Run 2 ATLAS displaced leptons search [22] for the estimation of backgrounds from fake and heavy-flavor (FHF) leptons and cosmic ray muons. The ABCD search is performed in two orthogonal sets of signal regions (SRs) with different triggers and lepton p_T thresholds. The "high-p_T" SRs use a similar selection as the prior Run 2 search [22], and the new large radius tracking (LRT) SRs use novel Run 3 triggers that employ LRT [31] (Section 2.2) to extend the trigger tracking to large transverse impact parameter ($|d_0|$) values, thus enabling reduced lepton thresholds with respect to Run 2. A separate "EM-BDT" search also exploits the new LRT trigger for electrons, and leverages precision tracking and electromagnetic calorimeter information (Section 2.3) to improve the displaced e/γ selection, building on previous ATLAS Run 2 searches for displaced photons [32, 33]. The LRT channel of the ABCD search and the EM-BDT search both use 56.3 fb^{-1} of Run 3 data collected at $\sqrt{s}$ = 13.6 TeV in 2022–2023, while the ABCD high-p_T channel also uses the full Run 2 dataset of 140 fb^{-1} collected at $\sqrt{s}$ = 13 TeV.

The paper is organized as follows. Section 2 describes the ATLAS detector, with specific emphasis on the unique LRT and LAr reconstruction techniques employed in the analysis. Section 3 describes the data and simulated samples used, and selections for objects and analysis events are given in Section 4. Descriptions of the ABCD (Section 5) and EM-BDT (Section 6) analyses follow, including detailed event selections, background estimations, and systematic uncertainties. Finally, results and interpretations are presented in Section 8, followed by brief conclusions.

2 ATLAS detector

The ATLAS detector [34, 35] at the LHC covers nearly the entire solid angle around the collision point.[1] It consists of an inner tracking detector surrounded by a thin superconducting solenoid, electromagnetic and hadronic calorimeters, and a muon spectrometer incorporating three large superconducting air-core toroidal magnet systems.

---

[1] ATLAS uses a right-handed coordinate system with its origin at the nominal interaction point (IP) in the center of the detector and the z-axis along the beam pipe. The x-axis points from the IP to the center of the LHC ring, and the y-axis points upwards. Polar coordinates (r, ϕ) are used in the transverse plane, ϕ being the azimuthal angle around the z-axis. The pseudorapidity is defined in terms of the polar angle θ as $\eta = -\ln\tan(\theta/2)$ and is equal to the rapidity $y = \frac{1}{2}\ln\left(\frac{E+p_z c}{E-p_z c}\right)$ in the relativistic limit. Angular distance is measured in units of $\Delta R \equiv \sqrt{(\Delta y)^2 + (\Delta \phi)^2}$.

2.1 Detector subsystems

The inner-detector system (ID) is immersed in a 2 T axial magnetic field and provides charged-particle tracking in the range $|\eta| < 2.5$. The high-granularity silicon pixel detector covers the interaction region and typically provides four measurements per track, the first hit generally being in the insertable B-layer (IBL). It is followed by the SemiConductor Tracker (SCT), which usually provides eight measurements per track. These silicon detectors are complemented by the transition radiation tracker (TRT), which enables radially extended track reconstruction up to $|\eta| = 2.0$. The TRT also provides electron identification information based on the fraction of hits (typically 30 in total) above a higher energy-deposit threshold corresponding to transition radiation.

The calorimeter system covers the pseudorapidity range $|\eta| < 4.9$. Within the region $|\eta| < 3.2$, EM calorimetry is provided by barrel and endcap high-granularity lead/LAr calorimeters, with an additional thin LAr presampler covering $|\eta| < 1.8$ to correct for energy loss in material upstream of the calorimeters. Hadronic calorimetry is provided by the steel/scintillator-tile calorimeter, segmented into three barrel structures within $|\eta| < 1.7$, and two copper/LAr hadronic endcap calorimeters. The solid angle coverage is completed with forward copper/LAr and tungsten/LAr calorimeter modules optimized for electromagnetic and hadronic energy measurements, respectively.

The muon spectrometer (MS) comprises separate trigger and high-precision tracking chambers measuring the deflection of muons in a magnetic field generated by the superconducting air-core toroidal magnets. The field integral of the toroids ranges between 2.0 and 6.0 T m across most of the detector. Three layers of precision chambers, each consisting of layers of monitored drift tubes, cover the region $|\eta| < 2.7$, except in the innermost layer of the end-cap region, where layers of small-strip thin-gap chambers and Micromegas chambers both provide precision tracking in the region $1.3 < |\eta| < 2.7$. The muon trigger system covers the range $|\eta| < 2.4$ with resistive-plate chambers in the barrel, thin-gap chambers in the endcap regions, and the aforementioned small-strip thin-gap chambers and Micromegas chambers in the innermost layer of the endcap. These replaced cathode-strip chambers that were used through Run 2.

The luminosity is measured mainly by the LUCID–2 detector that records Cherenkov light produced in the quartz windows of photomultipliers located close to the beampipe.

Events are selected by the first-level trigger system implemented in custom hardware, followed by selections made by algorithms implemented in software in the HLT [36]. The first-level trigger accepts events from the 40 MHz bunch crossings at a rate below 100 kHz, which the high-level trigger further reduces in order to record complete events to disk at an average rate of about 1 (3) kHz in Run 2 (3).

The Run-3 detector configuration benefits from several upgrades compared with that of Run 2 to maintain high detector performance at the higher pileup levels of Run 3. The improvements include a new innermost layer of the muon spectrometer in the end-cap region, which provides higher redundancy and a large reduction in fake muon triggers. The trigger system also benefits from new LAr digital electronics with significantly increased granularity. Other updates and further details are provided in Ref. [35]. A software suite [37, 38] is used in data simulation, in the reconstruction and analysis of real and simulated data, in detector operations, and in the trigger and data acquisition systems of the experiment.

As described in more detail below, this analysis exploits some specialized capabilities of the ATLAS detector and its TDAQ system. These include LRT (see Section 2.2), which is the ability to reconstruct tracks with a large impact parameter with respect to the PV, and the ability of the EM calorimeter to measure the flight direction and time-of-arrival of particles causing EM showers (see Section 2.3).
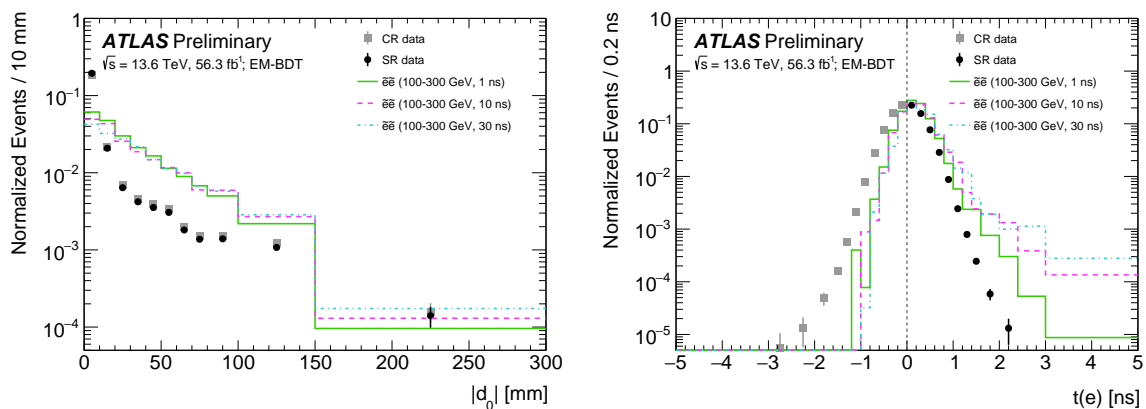
Figure 2: Representative data and signal model distribution for the (left) $|d_0|$ and (right) LAr timing distribution using the EM-BDT search regions, for Run 3 data and selected signal samples. The LAr timing measurement has been calibrated to zero for promptly produced particles traveling near the speed of light. The data events with negative times (gray squares) represent the signal-depleted control region (CR) used to determine the background estimate, while the data events with positive times (black circles) represent the signal region (SR) events on which the final search is performed. The SR data were blinded until the analysis strategy was finalized and the data were unblinded to determine the results.

2.2 Large radius tracking

The standard ATLAS tracking algorithm is designed to reconstruct the trajectory of promptly produced charged particles. It is efficient out to a $|d_0|$ of approximately 5 mm, limiting its usefulness for LLPs that decay to charged particles after traversing part of the detector. LRT [39] is a configuration of the tracking algorithm designed to increase the tracking efficiency for decay products of LLPs. The left panel of Figure 2 shows an example $|d_0|$ distribution, extending well past 5 mm, for several models in the EM-BDT search, which combines both standard and LRT tracking. For the offline reconstruction of data, it is implemented as a second-pass, running on the remaining hits that were not used by the standard tracking, with a looser restriction on the impact parameters and other optimizations, e.g. in the seeding step. Large radius tracks are reconstructed out to a $|d_0|$ of 300 mm, the first layer of the SCT. Compared to previous searches during Run 2, the LRT configuration in the reconstruction software has been improved to greatly reduce the number of incorrectly reconstructed tracks as well as to reduce the computation time, allowing LRT tracks to be reconstructed in all events.

In Run 3, LRT is run in the HLT for the first time [31]. For signal-like electrons and muons, the LRT used in the HLT is expected to be more than 80% efficient with respect to offline reconstruction for $|d_0| < 125$ mm. This is possible due to improvements in the LRT computation time, the HLT tracking algorithms, and the HLT computing resources. LRT for leptons in the trigger is implemented as a single pass, running on all hits in small regions around lepton candidates from the first-level trigger, with the same looser restrictions on impact parameters and similar optimizations as the offline reconstruction.

2.3 Electromagnetic calorimeter timing and pointing measurements

Electrons from the decays of massive LLPs could reach the LAr calorimeter with a slight delay compared to prompt electrons. This delay arises mostly from the LLP time-of-flight, which corresponds to a relativistic

speed ($\beta = v/c$) that can be substantially less than one.

In addition, the opening angle in the LLP decay causes the electron to be "non-pointing", arriving at the calorimeter from a direction that does not point directly back to the PV. This effect results in the geometrical path to the calorimeter being longer than that for a prompt electron from the PV, further increasing the delay in its arrival time. The right panel of Figure 2 illustrates the delay in the timing distribution of several signal models in the EM-BDT SR.

As described in Refs. [32, 33] and references therein, the fine segmentation of the LAr EM calorimeter can be used to measure the flight direction of a particle (electron or photon) that produces an EM shower, while its accordion structure and fast readout allows precise measurement of the particle's arrival time at the calorimeter. A line drawn through the centroids of the EM shower in the first two longitudinal layers is used to calculate the pointing value, defined as the difference between the position on the z-axis where the line crosses the beamline and the position of the PV. The resolution on the pointing measurement is ≈ 15 mm for an EM shower with energy of ≈ 50–100 GeV in the barrel. The arrival time is determined using the energy deposit from the second-layer EM calorimeter cell with the maximum energy deposit among cells in the associated EM shower ($E_{\text{cell}}^{\text{max}}$). For an electron with an energy in the range of interest, this cell typically contains about 20%–50% of the total energy deposited in the EM shower. The timing resolution is approximately 200 ps for EM showers with $E_{\text{cell}}^{\text{max}}$ greater than 20 GeV, and is dominated by the LHC beamspread.

3 Data and Simulation samples

Collision data collected by the ATLAS detector from the LHC's $\sqrt{s}$ = 13 TeV pp Run 2 (2015–2018) and $\sqrt{s}$ = 13.6 TeV pp Run 3 (2022–2023) are used. The ABCD high-p_{T} search uses the full Run 2 dataset of 140 fb^{-1} and 56.3 fb^{-1} of Run 3 data, obtained after detector conditions and data quality requirements [40] are applied. The uncertainty on the Run 2 integrated luminosity is 0.83% [41], for 2022 it is 2.2% [42], and for 2023 it is 2% [43], following the methodology discussed in Ref. [41], using the LUCID–2 detector [44] for the primary luminosity measurements, complemented by measurements using the inner detector and calorimeters. The ABCD LRT and EM-BDT searches use only the Run 3 data. Run 2 data was reconstructed with a consistent software suite [38] as used for Run 3 data to take advantage of developments, such as the improved LRT described in Section 2.2.

Data were collected with several triggers [36, 45] with signatures and thresholds that would accept events from displaced decays of leptons. Electron [46] and muon [47] triggers based on standard tracking [48] are efficient out to $|d_0|$ values of approximately 5 or 10 mm respectively. Thus they are not optimal for saving events with LLPs of moderate lifetime. Photon triggers accept events with electrons, even if they are too displaced to reconstruct a track, but have higher energy thresholds than electron triggers. MS-only triggers accept events based on muon tracks in the MS, without the need for an inner-detector track; these also have higher thresholds and some have restrictions in η to additionally reduce the trigger rate. Thanks to the requirement of an inner detector track, LRT-based lepton triggers are able to save events with lower momentum thresholds of 30 and 20 GeV for electrons and muons, with $|d_0|$ thresholds of 3 and 2 mm, respectively. Table 1 lists the triggers used based on the analysis region and lepton topology.

For the baseline GMSB-motivated slepton signal model in Figure 1, MC simulation events are used to determine the lepton selection criteria and estimate the sensitivity in a simplified GMSB SUSY model with light sleptons and a 1 GeV gravitino LSP. The signal models are given by the slepton flavor, mass, and

Table 1: Summary of trigger thresholds used for the ABCD and EM-BDT analyses, based on the object topology. Trigger objects are denoted as γ for photons, e for electrons, and μ for muons, preceded by the multiplicity and followed by the p_{T} threshold in GeV. MS-only indicates triggers that only rely on the Muon Spectrometer (MS), and not the inner detector. Trigger names contain the number of objects, the type of the object, and its p_{T} threshold. For example, $2\gamma50$ means a trigger requiring the presence of two photons with $p_{\mathrm{T}} > 50$ GeV. The $1\mu60$ MS-only trigger has a restriction of $|\eta| < 1.05$. The large radius tracking (LRT) electron (muon) trigger has a $|d_0| > 3(2)$ mm requirement. None of the triggers have an isolation requirement. "OR" indicates a logical OR of multiple triggers.

Topology	Trigger Thresholds [GeV]
ABCD High-p_{T}	
if $\geq 1e$, $p_{\mathrm{T}} > 160$ GeV	$1\gamma140$
else if $\geq 2e$, $p_{\mathrm{T}} > 60$ GeV	$2\gamma50$
else if $\geq 1\mu$, $p_{\mathrm{T}} > 60$ GeV, $|\eta| < 1.07$	$1\mu60$ (MS-only)
else if $e\mu$ (Run 3 only)	$\gamma40\mu40$ (MS-only)
else if $\mu\mu$ (Run 3 only)	$2\mu50$ (MS-only)
ABCD LRT	
e, $p_{\mathrm{T}} > 31$ GeV	$1e30$ (LRT)
μ, $p_{\mathrm{T}} > 21$ GeV	$1\mu20$ (LRT)
EM-BDT	
$= 1e, 0\gamma$	$1e30$ (LRT) OR $1\gamma140$
$\geq 2e$ OR $(1e, 1\gamma)$	$1e30$ (LRT) OR $2\gamma50$ OR $1\gamma140$
$\geq 2\gamma$	$2\gamma50$ OR $1\gamma140$

lifetime. For each slepton mass value, several slepton lifetimes were simulated, typically ranging from 1 ps to 30 ns. Since the distribution of particle flight distances follows an exponential distribution, it is possible to reweight the shape of that curve and thus generalize from the simulated samples to other lifetime values. Each event is assigned a weight according to a source signal lifetime, target signal lifetime, and the decay of the event in question.

Signal model MC simulation events with up to two additional partons at leading order are generated using MadGraph5_aMC@NLO v2.6.1 [49] interfaced to Pythia 8.230 [50] with the A14 parameter set (tune) [51] along with the NNPDF2.3lo parton distribution function (PDF) set [52]. Geant4 [53] is used to simulate the propagation and decay of the slepton without preserving information about its chirality. To model the impact of multiple interactions that occur in the same and neighboring bunch crossings (pile-up), each hard-scattering event is overlaid [54] with simulated minimum bias events generated by EPOS 2.0.1.4 [55, 56] with the EPOS LHC tune and PYTHIA 8.307 with the NNPDF2.3 LO set of PDFs and A3 tune [57]. The 13 TeV slepton-pair production cross sections and uncertainties were calculated at next-to-leading-order in α_{s}, with soft-gluon emission effects at next-to-leading-logarithm [58–62]. At 13.6 TeV, these were calculated at approximate next-to-next-to-leading-order in α_{s} matched with threshold resummation at the next-to-next-to-leading logarithmic accuracy (aNNLO+NNLL) using an envelope of predictions with different factorization and renormalization scales and PDF sets [63]. The superpartners of the left- and right-handed leptons are assumed to have equal mass. The slepton-pair cross section for a single flavor of $\tilde{\ell}$ with mass 100 GeV (800 GeV) is 0.37 ± 0.01 pb (0.059 ± 0.004 fb) at 13 TeV and 0.41 ± 0.01 pb (0.069 ± 0.008 fb) at 13.6 TeV.

4 Object selections and event preselections

The main objects used in this analysis are electrons and muons, including those produced in the decays of tau leptons, and photons. Jets, including those from hadronically-decaying tau leptons, are also used in the procedure to remove ambiguities between nearby reconstructed objects ("overlap removal") and to construct the magnitude of the missing transverse momentum (E_T^{miss}), which is used in the EM-BDT analysis.

For electrons, muons, and photons, a baseline selection is used for the overlap removal procedure. For electrons and muons, additional kinematic requirements are imposed before separating events into the ABCD and EM-BDT regions; these are referred to as high-d_0 leptons in the paragraphs below. Analysis dependent selections are then applied to high-d_0 leptons to define signal leptons that are used to construct SRs, which are used to search for signal-like excesses above SM expectations.

Electrons are reconstructed from ID tracks matched to clusters of energy deposited in the EM calorimeter. If a standard and large radius track both point to the same EM cluster and lead to the reconstruction of a standard and LRT electron with the same cluster, the electron passing the stricter identification requirement is kept, and in case of a tie, the electron reconstructed with a standard track is kept. Baseline electrons must have $p_T > 10$ GeV, $|\eta| < 2.47$, and pass a modified version of the *VeryLoose* identification working point (WP) [64] that does not depend on $|d_0|$, $|d_0|$ significance, or the number of Pixel hits, to avoid suppressing displaced electrons, referred to here as LLP VeryLoose. The left panel of Figure 3 shows the efficiency of electrons from a selectron signal model to pass the standard and LLP electron ID WP as a function of the true lepton $|d_0|$ value.

High-d_0 electrons, for the purpose of analysis region definition, must additionally pass the object overlap removal, satisfy $p_T > 31$ GeV, $3 < |d_0| < 300$ mm, $|z_0| < 500$ mm, and fall outside of the EM calorimeter barrel-endcap gap ($1.37 < |\eta| < 1.52$). The ABCD signal electron selection additionally requires that the electrons are isolated from nearby tracks and calorimeter energy deposits. The sum of the p_T of all tracks within $\Delta R = 0.2$ and E_T of all energy depositions within $\Delta R = 0.3$ of the electron must each be less than 6% of the electron p_T. To suppress electrons from random overlaps of hadronic tracks and photon energy depositions, the relative difference between the electron track p_T measurement and that of the electron p_T measured when accounting for the calorimeter energy must satisfy $(p_T^{\text{track}} - p_T^e)/p_T^e \equiv \Delta p_T \geq -0.5$. To suppress combinatoric fake tracks, the ID track must have a χ^2 per degree of freedom satisfying $\chi^2_{\text{ID}}/\text{n.d.f.} < 2$, where χ^2 is the sum of the squares of the distances between each hit and the track position extrapolated to the given sensor divided by the resolution on this difference, and at most one missing cluster that is included in the track fit (track "hit") at a larger radius than the innermost hit. Signal electrons in regions triggered by the LRT trigger require the stricter LLP Loose identification WP to be consistent with the trigger, with the same modifications as above to the standard *Loose* WP [64]. The EM-BDT signal electron selection requires the baseline selection, $3 < |d_0| < 300$ mm, the same isolation criterion, and the same LLP *Loose* identification WP.

Muons are reconstructed from ID tracks matched to muon track segments. If a standard and LRT track both point to the same muon segment and lead to the reconstruction of a standard and LRT muon with the same segment, the duplication is resolved by keeping the muon with the smaller difference in η between the ID track and the muon track segment extrapolated to the PV. Baseline muons must have $p_T > 21$ GeV, $|\eta| < 2.5$, and pass a modified version of the *Medium* identification WP [65] without requirements on the number of Pixel and TRT hits. The right panel of Figure 3 shows the efficiency of muons from a smuon

signal model to pass the standard and LLP muon medium ID WP as a function of the true lepton $|d_0|$ value.

High-d_0 muons must additionally satisfy the object overlap removal, $2 < |d_0| < 300\,\text{mm}$, and $|z_0| < 500\,\text{mm}$. Signal muons are required to additionally be isolated from nearby tracks and calorimeter energy depositions using an algorithm that exploits Particle-Flow to associate tracks with their energy clusters [65]. The sum of the p_T of within $\Delta R = 0.3$ of the muon is added to 40% of the sum of the E_T of energy depositions within $\Delta R = 0.2$ that aren't matched to tracks and required to be less than 16% of the muon p_T. Several additional requirements are imposed to reject spurious muons from combinatoric fake tracks. Muons must be measured in at least three MS precision tracking layers and have at least one high-precision ϕ measurement. The ID track must have $\chi^2_{\text{ID}}/\text{n.d.f.} < 2$ and at most one missing hit at a larger radius than the innermost hit, and the combined muon track must satisfy $\chi^2_{\text{CB}}/\text{n.d.f.} < 3$. To reject cosmic-ray muons, a cosmic muon veto is applied that is similar to the one used in the ATLAS Run 2 displaced leptons search [22] and originally developed in the ATLAS Run 2 search for a displaced vertex and a displaced muon [66]. A muon is tagged as originating from a cosmic-ray muon, and thus vetoed, if there are MS segments on the opposite side of the detector along its trajectory, within η and ϕ windows of $|\eta_\mu + \eta_{\text{MS}}| < 0.01$ and $\pi - |\phi_\mu - \phi_{\text{MS}}| < 0.08$, where the μ and MS subscripts refer to the reconstructed muon and MS segments, respectively.

Photons are reconstructed from EM calorimeter depositions. Baseline photons must have $p_T > 30\,\text{GeV}$, fall within the barrel ($|\eta| < 1.37$) or endcap ($1.52 < |\eta| < 2.5$) regions, and pass the *Loose* photon identification WP [64]. Signal photons must also be isolated from nearby tracks and calorimeter depositions [64]. The sum of the p_T of all tracks (E_T of all energy depositions) within $\Delta R = 0.2$ of the photon must be less than 5% (6.5%) of the photon p_T.

Jets are reconstructed with the Particle Flow technique [67] using the anti$-k_t$ algorithm with a radius parameter of 0.4 [68]. In this analysis, jets are only used for overlap removal and, for the EM-BDT search only, to evaluate the E_T^{miss}. Baseline jets must satisfy $p_T > 20\,\text{GeV}$ and $|\eta| < 2.8$. To reject jets from pile-up interactions, a Jet Vertex Tagger algorithm employing a neural network is applied using a WP with an approximately fixed efficiency as a function of jet p_T [69].

The value of E_T^{miss} is defined as the magnitude of the negative vector sum of the transverse momenta of all distinct reconstructed objects as well as tracks not associated to any reconstructed objects. When calculating the value of E_T^{miss}, both prompt and displaced leptons are included.

The analysis requires one of the following three conditions to be true: at least one baseline electron, at least two baseline muons, or at least two baseline photons. Events must pass one of the triggers described in Section 3, which depend on the final state and the p_T of the leptons and photons. During 2023, part of the TRT barrel was not in operation, in a region defined by $-1.759 < \phi < -1.257$ and $|\eta| < 1.37$. Events with electrons or muons in this $\eta - \phi$ region are vetoed in 2023 data only.

Events are categorized into orthogonal ABCD high-p_T, ABCD LRT, and EM-BDT regions in cascading order based on the number of high-d_0 leptons, as defined above. If there are at least two such leptons with $p_T > 65\,\text{GeV}$, events fall into the ABCD high-p_T regions. Failing that, if events have at least two such leptons with $p_T > 31(21)\,\text{GeV}$ for electrons (muons), events fall into the ABCD LRT regions. Remaining events fall into the EM-BDT regions. Additional selections, defined in Sections 5 and 6 for the ABCD and EM-BDT approaches, respectively, are used to define SRs that are sensitive to BSM signals, control regions (CRs) that are used to estimate the backgrounds in the SRs, and validation regions (VRs) that are used to test the robustness of the background estimation methodology. The SRs, CRs, and VRs for each channel are mutually orthogonal.
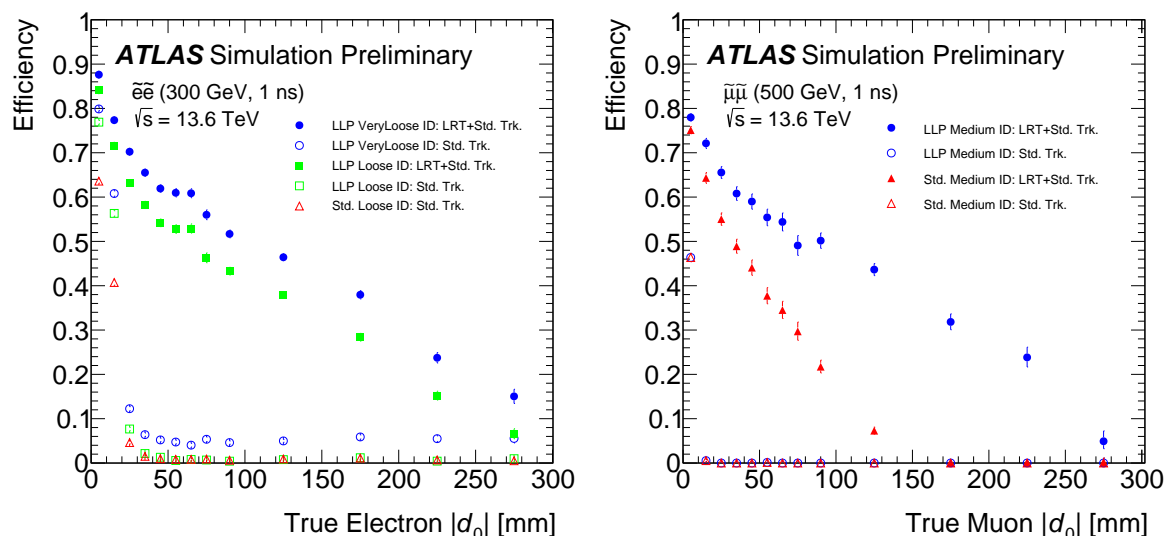
Figure 3: Efficiency to reconstruct and identify electrons (left) and muons (right) using large radius tracking (LRT) and standard tracking (Std.) with respect to MC generator-level leptons in a simulated GMSB slepton signal models, namely with a slepton mass and lifetime of 300 GeV and 1 ns, respectively. The efficiencies for the various LLP WP are shown as a function of the true transverse impact parameter $|d_0|$ of the daughter lepton.

5 ABCD analysis

The ABCD analysis defines SRs for three dilepton flavor combinations, ee, $\mu\mu$, and $e\mu$, using the flavors of the two leptons with the highest p_T. Backgrounds are estimated using two ABCD-based estimations, one for FHF leptons and one for cosmic ray muons, which make use of leptons passing and failing certain quality criteria. Cosmics ray muons are only relevant for the $\mu\mu$ final state. Region A, shared for the FHF and cosmic ray muon estimate, is the SR where both leptons pass all analysis requirements, regions B and C have only one lepton passing the criteria and the other fails, and region D contains events where both leptons fail the criteria, which are different for the FHF and cosmic ray muon estimate. When the criteria used on each lepton are uncorrelated, the estimate of the background in the SRs reduces to

$$N_A^{\text{predicted}} = \frac{N_B^{\text{FHF}} \times N_C^{\text{FHF}}}{N_D^{\text{FHF}}} + \frac{N_B^{\text{Cosmics}} \times N_C^{\text{Cosmics}}}{N_D^{\text{Cosmics}}},$$

where $N_{B/C/D}^{\text{FHF}}$ and $N_{B/C/D}^{\text{Cosmics}}$ are the event yields in the various control regions for the FHF and cosmic ray backgrounds, respectively, for a given lepton flavor combination. The BCD regions for a given SR are included in the fits to determine the backgrounds for model-independent limits and BSM exclusions, as described further in Section 8.

5.1 ABCD event selection

The selection of events for the ABCD analysis begins with the common preselection requirements described in Section 4. The ABCD search requires the presence of at least two signal leptons (e or μ) separated by $\Delta R(\ell_1, \ell_2) > 0.2$ and considers two orthogonal sets of SRs. The high-p_T SRs use a similar selection as the Run 2 search, relying on photon and MS-only muon triggers and requiring both leptons to have

10

$p_T > 65$ GeV and $|d_0| > 3$ mm. The Run 3 high-p_T SRs benefit from the addition of new photon plus MS-only and di-MS-only-muon triggers, listed in Table 1. Separate SRs are defined for ee, $\mu\mu$, and $e\mu$ events in Run 2 and Run 3, resulting in six orthogonal ABCD high-p_T SRs.

The ABCD LRT SRs use the novel LRT triggers that were introduced in Run 3 and require electrons (muons) with $p_T > 31$ (21) GeV. The muon $|d_0|$ threshold is also reduced to 2 mm. Electrons are required to pass the stricter LLP Loose WP to be consistent with the LRT trigger. Events satisfying the high-p_T SR selection are vetoed. Three SRs exploiting the LRT triggers are defined for ee, $\mu\mu$, and $e\mu$ events, in Run 3 only, leading to a total of nine orthogonal SRs considered in the ABCD search. For the three $\mu\mu$ SRs, an additional cosmic ray veto rejects events with back-to-back fully-reconstructed muons, μ_1 and μ_2, with $|\eta(\mu_1) + \eta(\mu_2)| < 0.02$ and $\pi - |\phi(\mu_1) - \phi(\mu_2)| < 0.01$, taking advantage of the better angular resolution of fully-reconstructed muons at the PV, compared to extrapolated MS segments.

To maintain broad sensitivity to BSM physics scenarios besides the baseline GMSB long-lived slepton considered in this paper, no additional kinematic selections are applied. Due to the low rates of displaced leptons in data, these selection criteria are sufficient to reduce the expected background yields in all SRs to less than an event.

5.2 ABCD background estimation

Two sources of background are considered in the ABCD analyses. The FHF lepton background contributes to all three lepton flavor channels and includes combinatoric fake tracks, random overlaps of hadronic tracks with EM clusters or MS tracks, photon conversions, and decays of heavy-flavor bottom and charm mesons. The cosmic-ray muon background contributes to $\mu\mu$ events only. Since these processes are not necessarily well-modeled in simulation, they are estimated from data CRs using ABCD methods that closely follow the methodologies of the Run 2 ATLAS displaced leptons search [22]. The final background estimates and results for each SR are obtained from a simultaneous fit of the four ABCD regions.

The background estimate for FHF leptons uses CRs in which some of the quality criteria on one lepton, or the other lepton, or both, are inverted. A failing electron is one that fails at least one of the requirements on Δp_T, ID track χ^2_{ID}/n.d.f., and the number of missing track hits, while satisfying all other ABCD signal electron requirements of Section 4. A failing muon is one that fails at least one of the requirements on the number of precision tracking layers, the presence of a high-precision ϕ measurement, ID track χ^2_{ID}/n.d.f., combined muon χ^2_{CB}/n.d.f., and the number of missing track hits, while satisfying all other ABCD signal muon requirements of Section 4. In the $\mu\mu$ high-p_T regions only, the observed yields in the ABCD CRs are too small to provide individual predictions for Run 2 and Run 3. Therefore the yields in the ABCD regions for these two datasets are combined and the predicted FHF background is scaled by the fractions of the total luminosity accounted for by each dataset; namely 0.71 for Run 2 and 0.29 for Run 3. The predicted SM background yields in each of the nine ABCD SRs is less than 0.2 events.

This method assumes that the quality criteria of the two FHF leptons are uncorrelated with each other. Two sets of VRs are defined to account for any systematic biases of the background estimation methodology, including potential correlations between the quality criteria of the the leptons. The VR-fake regions are enriched in fake lepton backgrounds by inverting the requirement on Δp_T for electrons and the CB track χ^2_{CB}/n.d.f. requirement for muons. The VR-HF regions are enriched in heavy-flavor leptons by inverting the lepton isolation criteria. The observed yields in the nine VR-fake and VR-HF regions corresponding to the nine SRs are consistent with the background expectations obtained by performing the ABCD estimate in these VRs.

For cosmic ray muons, the ABCD CRs are defined by inverting the MS quality requirements (number of precision tracking layers, number of high-precision ϕ measurements, or combined muon $\chi^2_{\mathrm{CB}}/\mathrm{n.d.f.}$) or by inverting the cosmic veto relying on the presence of MS segments on the opposite side of the detector. These are inverted for the muon in the top half of the detector, which is more likely to be mis-reconstructed than the muon in the bottom half since it travels in the opposite direction of particles that originate from the PV. Applying the additional cosmic ray veto on back-to-back fully-reconstructed muons eliminates almost all of the events in these regions. We therefore estimate the cosmic ray muon background without this additional cosmic ray veto applied and then scale the result by the expected efficiency $T = (3.7 \pm 2.6) \times 10^{-3}$ for muons to survive this veto, evaluated using the events that fall in the superset of regions B, C, and D. The expected background yields are of order 10^{-3} in the three $\mu\mu$ SRs.

This background method is validated in VRs enriched in cosmic ray muons, in which the cosmic veto relying on the presence of MS segments on the opposite side of the detector as the bottom muon is replaced by the requirement that this muon has MS segments satisfying $|\eta_\mu + \eta_{\mathrm{MS}}| < 0.01$ and $\pi - |\phi_\mu - \phi_{\mathrm{MS}}| < 0.08$ but no such segments satisfying $|\eta_\mu + \eta_{\mathrm{MS}}| < 0.002$ and $\pi - |\phi_\mu - \phi_{\mathrm{MS}}| < 0.02$. To enrich the VR in cosmic ray muons, the additional cosmic ray veto based on the two fully-reconstructed muons is not applied. The observed yields are consistent with the background expectations.

5.3 ABCD systematic uncertainties

While the sensitivity of the ABCD analysis is dominated by statistical uncertainties, several sources of systematic uncertainty are considered. Additional uncertainties common with the EM-BDT analysis are described in Section 7.

The systematic uncertainty on the FHF lepton background is based on the agreement between observed yields versus expected backgrounds in the VR-fake and VR-HF regions. For each region, the larger of two quantities is taken as the systematic uncertainty: the deviation from one of the ratio of the observed yield to the expected background, or the statistical uncertainty on the expected background. The values are extracted from VR-fake and VR-HF separately and then added in quadrature. Uncertainties in the range (20–240)% are applied in the corresponding SRs, with the larger uncertainties occurring in regions with very small observed yields.

Two sources of systematic uncertainty on the cosmic ray muon background are considered. The first source is due to the assumption that the muon in the top half of the detector is the one that is mismeasured. The background is estimated by instead inverting the cosmic veto and/or MS quality variables of the bottom muon and taking the relative difference with respect to the nominal result, resulting in uncertainties of (2–41)%. The cosmic ray background is also estimated by inverting any two of the three MS quality variables and take the relative difference with respect to the nominal estimate, resulting in uncertainties of (20–82)%.

6 EM-BDT analysis

The EM-BDT analysis seeks to discriminate between displaced electrons and the background, which is dominated by prompt particles. In the interpretation of the results for the GMSB long-lived slepton model used as a benchmark (see the diagram in Figure 1), the EM-BDT analysis is applied to the selectron and stau channels, since either can produce displaced electrons in the final state.

As an electron arising from the decay of a long-lived parent is both displaced and delayed, there exist significant correlations between a number of relevant observables, motivating the introduction of machine learning (ML) techniques in the development of a multivariate discriminant. An electron from an LLP decay that occurs too far into the detector may not have an identifiable track. In such a case, the electron will be reconstructed as a photon, provided the decay is before the calorimeter. Two different BDTs are employed, each using variables that are verified with comparisons of $Z \rightarrow ee$ data and MC simulation to be reasonably well modeled. The "eBDT" seeks to identify displaced electrons from among those particles reconstructed as electrons, while the "γBDT" seeks to identify displaced electrons from among those particles initially reconstructed as photons. The γBDT extends the sensitivity of the analysis to events where the decay producing the electron occurs in front of the EM calorimeter but farther from the beamline than the 300 mm limit where LRT is applied; in such cases, it is still possible to identify the displaced electron from the EM calorimeter information only.

The discriminating variables for the eBDT include tracking information, EM calorimeter variables, and combinations of the ID and LAr measurements. The tracking variables include the track fit quality χ^2 value, the number of pixel hits on the track, the number of missing layers in the track, and the transverse ($|d_0|$) and longitudinal (z_0) impact parameters with respect to the PV position. The EM calorimeter variables include the LAr pointing measurement, the absolute value of the LAr timing measurement, and two LAr shower shape variables, namely the fraction of the EM shower energy in the first and third longitudinal layers (f_1 and f_3, respectively.). The combined variables include Δp_{T}, the difference between track pointing (z) and LAr pointing (z_{EM}); both of these combined variables are intended to help reject backgrounds from fake electrons. The background rejection of the eBDT is sufficient that the analysis can be performed with only one reconstructed electron in the event, thereby greatly extending the analysis sensitivity to longer slepton lifetime values, where only one selectron (or stau) has decayed before reaching the EM calorimeter. In events with more than one reconstructed electron, or with one electron and one or more photons, the eBDT is applied to the leading electron. Thus, the eBDT is an "object-level" discriminant, using only measurements of the electron itself and not of other properties of the event, and thereby functions as a "displaced electron tagger". This feature of the eBDT makes it rather model-independent.

The γBDT searches for displaced electrons reconstructed as photons. The lack of tracking information and higher background rates for photons than electrons makes a single photon region infeasible. Instead, the γBDT requires at least two photons. The variables used are the pointing and timing measurements of the two photons, as well as the differences between them. In addition, the value of $E_{\mathrm{T}}^{\mathrm{miss}}$ in the event is used; this choice targets exploiting the gravitinos produced in the baseline slepton model to extend the reach of the analysis to longer slepton lifetime values, with more displaced decays, but does make the γBDT more model-dependent than the eBDT.

6.1 EM-BDT event selection

The selection of events for the EM-BDT analysis begins with the common preselection requirements described in Section 4. The EM-BDT event selection is made orthogonal to that of the ABCD analysis regions by vetoing dielectron events passing the ABCD p_{T} and $|d_0|$ requirements. The selected EM-BDT events are divided into several distinct final states, according to the multiplicity of reconstructed EM objects (electrons or photons) in the event. Each final state is selected by a set of triggers, as described in Table 1.

The eBDT is used to analyze events with at least one electron in the barrel calorimeter ($|\eta| < 1.37$). These include single-electron events, but also events with an electron in the barrel calorimeter plus either

additional electrons or photons. In events with more than one reconstructed electron, the leading electron in the barrel is selected as the input object to the eBDT algorithm. The electron is required to have $E_{\text{cell}}^{\text{max}} > 5$ GeV to reduce the impact of noise on the calorimeter timing, and an absolute value of its calorimeter time less than 12.5 ns, to reject backgrounds from other bunch crossings.

Given the large backgrounds in single-photon event samples as well as the lack of tracking information for photons, the γBDT is used to analyze only events with at least two reconstructed EM objects; the first must be a photon passing the baseline requirement, while the second can be another photon or an electron which fails the eBDT requirements. At least one EM object must be in the barrel calorimeter ($|\eta| < 1.37$). Both EM objects are required to have $E_{\text{cell}}^{\text{max}} > 5$ GeV and an absolute value of its calorimeter time less than 12.5 ns. A requirement of $|z| < 2000$ mm for both EM objects eliminates beam-induced backgrounds which can fake the photon signature.

6.2 EM-BDT background estimation

The background to the EM-BDT analysis is dominated by prompt particles which are mismeasured or poorly reconstructed. Such effects cannot be sufficiently precisely simulated, and therefore the background estimation is necessarily entirely data-driven. The estimate is generated by dividing the data into three orthogonal regions: a CR with < 1% signal contamination, which can be used to generate the estimate of the background normalization and BDT shape, a VR, also with < 1% signal contamination, which can be used to validate the background estimate before unblinding the SR data, and the SR, in which the search will ultimately be performed.

The EM-BDT analysis exploits the fact that, for prompt background, the distribution of the arrival time at the EM calorimeter should, due to resolution effects, be symmetric about zero (as seen in Figure 2). In contrast, signal events should be delayed, and therefore primarily have positive arrival times. As a result, the CR can be defined for the eBDT (γBDT) by events where the leading electron has (both photons have) a negative time, while the SR is defined by events where the leading electron has (both photons have) a positive time. The VR is defined by kinematic selections which aim to achieve a dominance of background over signal by selecting events with enhanced SM W or Z boson production; the VR includes single-electron events with a transverse mass in the range from 60–100 GeV, and dielectron events with a dielectron mass in the range from 80–100 GeV. To guarantee orthogonality among the three regions, the CR and SR definitions include vetoes of any events that fall within the VR selection.

For both the eBDT and the γBDT, the BDT is trained to separate the signal, as modeled with MC simulation, from the background, as modeled by the CR data. Signal models of various masses and lifetimes ≥ 1 ns were used for training in order to maximize sensitivity to longer lifetimes. To make use of the full statistics of the MC simulation and the CR data, the signal sample and data used for training are split randomly into three "folds" and training performed on each group individually. It is then required that the score assigned to a particular event during evaluation is determined using a fold other than the one assigned to that event in training. The final EM-BDT results for various signal models (i.e. values of slepton mass and lifetime) are obtained by signal-plus-background fits, including associated statistical and systematic uncertainties, of the unblinded SR data to the weighted sum of the CR-derived background template and signal template shape from MC simulation. Before unblinding the SR data, the BDT distributions were validated by performing fits to the (background-dominated) VR.

The BDTs are defined such that their output values range from -1 to +1, with signal-like (background-like) events skewed toward positive (negative) BDT scores. The final statistical analysis uses a simultaneous fit

to binned eBDT and γBDT distributions, where the normalization is allowed to float. Before unblinding, the binning used for the BDT scores was subject to an optimization procedure that sought to maximize the signal sensitivity. To ensure a non-zero background estimate could be made for each bin, the choice of bins was subject to the constraint that there exist at least one CR event in each bin. The eBDT and γBDT binnings were optimized separately. However, for both BDTs the very background-like events with BDT score less than zero are not used in the fit, and the events with positive BDT scores are divided into five non-overlapping bins.

6.3 EM-BDT systematic uncertainties

While the sensitivity of the EM-BDT analysis is dominated by statistical uncertainties, several sources of systematic uncertainty are considered. The background normalization is determined in the fit, and therefore no corresponding systematic uncertainty is needed. However, systematic uncertainties which are considered can impact the results of the final fit by either impacting the shapes of the BDT score distribution of the signal and/or the background, or by affecting only the signal normalization. Additional uncertainties common with the ABCD analysis are described in Section 7.

The largest systematic uncertainty on the shape of the background BDT distribution arises due to the assumption that the CR data, which has negative time values, describes accurately the expected background in the SR region, which has positive times. The systematic uncertainty on this assumption is determined by using the VR data, where the signal contribution is negligible and therefore the symmetry of the background around $t = 0$ ns can be tested quantitatively. Comparing the BDT distribution of the VR data with negative times with that of the VR data with positive times, the relative discrepancies increase monotonically toward the higher BDT score bins, and reach as high as 33% (84%) in the highest bin of the eBDT (γBDT) score. These "non-closure" uncertainties are symmetrized about the central prediction and included as systematic uncertainties on the BDT background shape.

A systematic uncertainty on the shape of the signal BDT distribution arises due to uncertainties on the smearing of the time resolution. The MC simulation does not accurately describe the timing resolution in data, and therefore the signal MC events are subjected to additional smearing of the time. The smearing procedure consists of taking the raw time from the MC simulation, which already contains a model of the observed noise in the calorimeter, and adding additional correlated and uncorrelated components. The correlated component corresponds to the beam spread, and is therefore shared by all objects in the same event. The uncorrelated component is applied separately to each object and corresponds to different electronic and pileup noise assumptions and other global effects observed in comparisons between data and MC simulation. To determine a systematic uncertainty on the resultant impact on the signal BDT shape, the smearing is varied up and down within the experimental uncertainties, and the signal BDT shape re-evaluated.

7 Common systematic uncertainties

Several sources of systematic uncertainties are evaluated for the prediction of signal model yields, both from the theory side and experimental side. The factorization and renormalization scales, α_S, parton distribution functions, and QCD radiation models are all varied to assess the impact on the simulated acceptance in the SRs. For the ABCD SRs, a 25% uncertainty is applied to cover these variations; while in

the EM-BDT SR a 12% uncertainty is applied. The uncertainty on the total predicted cross-section is not included as an additional uncertainty in the fit.

Experimental-based uncertainties on the modeling of leptons are determined in two parts. Electrons and muons are reconstructed with a track and calorimeter or MS information, respectively. These sub-detectors are sufficiently far from the PV relative to the displacements targeted in this search that the sub-detectors performance, and simulation of said performance, should not differ by much from that for prompt leptons. Thus uncertainties on the tracking and calorimeter or MS are separated in order to determine each in the most robust way. Additional uncertainties to take into account the nature of displaced leptons are added on top of uncertainties derived for prompt leptons, which cover the calorimeter and MS portion of the leptons. Standard uncertainties on the modeling of photons are included; there are no additional displacement based uncertainties applied for photons other than that describe for the smearing of the time resolution in Section 6.3.

Uncertainties on objects reconstructed in the final state are propagated to the reconstruction of E_T^{miss}. Additional uncertainties on E_T^{miss} come from varying the scale and resolution of the soft term, parallel and perpendicular to the hard term [70]. As E_T^{miss} is used in selecting events with enhanced SM W production to define the EM-BDT VR, a systematic is assessed on the impact of E_T^{miss}-reconstruction uncertainties on the fitted EM-BDT score distributions. The migration of events from EM-BDT SRs to the EM-BDT VR was studied after redefining the VR using variations in E_T^{miss}. Based on this a 2% uncertainty on the signal yields in the EM-BDT SRs was assigned. For the γBDT, which uses E_T^{miss} as an input variable, an additional uncertainty is evaluated by propagating the E_T^{miss} systematic uncertainties into the γBDT score calculation and re-evaluating the γBDT shape. Uncertainties on E_T^{miss} have no impact in the ABCD analysis since it is not used in the event selection.

The uncertainty on the modeling of LRT in offline reconstruction was determined from comparisons of data and MC simulation using K_S^0 vertices in Ref. [39]. These are parameterized in p_T and radius of the first hit on the track, and vary from 0.3–16.8% per large-radius track.

Uncertainties on the simulated acceptance of the trigger for standard prompt leptons and photons are considered. Additional uncertainties on the LRT-based trigger acceptance are computed by comparing the trigger tracking efficiency with respect to offline tracks in data and MC simulation, as in Ref. [45]. This amounts to an additional uncertainty of 11% for electrons and 2% for muons on top of the standard uncertainties.

Corrections the modeling of identification and isolation requirements for leptons were computed using prompt $Z \rightarrow \ell\ell$ events using the same methods as for electrons in Ref. [64] and muons in Ref. [65]. For electrons these are generally less than 11% for electrons with $p_T > 30$ GeV; they rise to 70% for electrons with $p_T < 20$ GeV. For muons these are generally less than 3%. An additional uncertainty on electron identification as a function of $|d_0|$ is assessed by comparing the relative loss in efficiency between the VeryLoose and Loose WPs of signal MC simulation; this amounts to an uncertainty of 16% per electron. The MS is sufficiently far away from the PV, and their identification does not make use of a likelihood discriminant, thus no additional displacement-based uncertainty is applied.

The uncertainties on the ABCD background predictions come from the propagation of statistical uncertainties on the yield in each region, which ranges from 20–120%, except for the High-p_T $\mu\mu$ regions where this is up to 1100%, and the uncertainties described in Section 5.3 on the FHF background prediction, which ranges from 30–210%. The dominant uncertainty on the signal prediction in the ABCD SRs depends on the region and signal model. Typical ranges for uncertainties are: 11–40% for the number of MC simulation events, 25% for the signal theory acceptance, 10–40% for the uncertainty on LRT, 1–15%

for muon modeling, and 20–30% for electron modeling. The uncertainty on the BDT backgrounds are dominated by the shape uncertainties, except for the most sensitive bin where the number of CR events is low and the statistical uncertainty is large. The dominant uncertainties for the eBDT are the electron modeling at 21%, the theory acceptance uncertainty at 12%, and the statistical uncertainty on the number of simulated events in the most sensitive bins at 7%. The dominant uncertainties for the γBDT are the signal acceptance uncertainty of 12%, and the statistical uncertainty on the number of simulated events in the two most sensitive bins at 11 and 4%. For both the ABCD and EM-BDT regions, the uncertainty on the lifetime reweighting may be the dominant uncertainty when used.

8 Results

Each of the orthogonal ABCD signal region is used individually to compare the observed data yield with the expected background, the results of which are used as "discovery regions" to set model-independent limits on the production of displaced leptons; for the ABCD high-p_T analyses, these are quoted separately for the Run 2 and Run 3 data, due to the different center-of-mass energies, resulting in a total of nine orthogonal ABCD discovery regions. An EM-BDT discovery region is defined as the most signal-like bin of the eBDT distribution (eBDT score > 0.46), and is used to set model-independent limits on the production of displaced electrons. All model-independent limits are derived using pseudo-experiments. Model-dependent limits on the long-lived slepton model, considered in Figure 1, are obtained by performing a simultaneous fit to the eBDT and γBDT distributions, as well as the nine ABCD SRs.

Only one event is observed among the nine orthogonal ABCD signal regions, namely in the SRee-LRT region. The observed and expected yields in the orthogonal ABCD signal regions are presented in Table 2. Corresponding model-independent upper limits on the effective BSM cross-sections, the observed and expected limits on the number of non-SM events, and the p-values and corresponding local Z scores are also shown. The one event observed in the SRee-LRT region, compared to the background expectation of $0.0016^{+0.0029}_{-0.0016}$ events corresponds to a local significance of 2.2σ.

The observed BDT distributions in the SRs of the eBDT and γBDT analyses are shown in Figure 4. Shown superimposed are the background shapes as determined using the CR data, and example GMSB signal models with selectrons. The lower panels in the figures show the bin-by-bin ratios of the data divided by the background, and illustrate the observed SR data are consistent with the background expectation. Defining the EM-BDT discovery region as the most signal-like bin of the eBDT yields a background expectation of 1 event. The uncertainty on this background estimate is dominated by the statistical uncertainty resulting from the fact it is determined from a single CR event in this bin of the eBDT, plus a systematic uncertainty of ±0.33 from the other sources of uncertainty described previously. A total of 3 events are observed in the EM-BDT discovery region, corresponding to a local significance of 0.9σ; this result is included as the last row of Table 2.

The combined ABCD and EM-BDT results are used to set exclusion contours on the GMSB stau and selectron models, in the two-dimensional plane of slepton lifetime versus slepton mass. The ABCD results only, are used for the smuon model as the EM-BDT is not sensitive to muons. The combination is obtained by simultaneously fitting all ABCD and EM-BDT distributions, using a single fit parameter to describe the signal strength. Thus the 13.6 TeV to 13 TeV cross-section ratio is taken from the theoretical prediction. To improve the interpolation between generated signal models with different lifetimes, a reweighting procedure is used to estimate the signal acceptances for lifetimes that were not included in the MC sample described in Section 3 and corresponding uncertainties on the signal yields are included in the fit. A 20% signal

normalization uncertainty was assessed for reweighting to lifetimes up to 100 ns, increasing to 50% for reweighting to even higher lifetimes, where the uncertainties are based on comparing reweighted samples to the same lifetime as a simulated sample.

The 95% CL exclusion contours for long-lived selectrons, smuons, and staus are shown in Figure 5. Results from the prior Run 2 analysis [22] are also included. The excluded regions from the current analysis extend to significantly higher slepton masses and much higher slepton lifetimes. For example, selectrons with a mass of 150 GeV are excluded for lifetime values ranging from 4 ps to 70 ns, while selectrons, smuons and staus with a lifetime of 0.3 ns are excluded up to 740 GeV, 840 GeV, and 380 GeV, respectively. The improvement in sensitivity for long lifetimes for selectrons with lower masses is due to the EM-BDT and new LRT-based triggers. For smuons, in addition to the LRT-based triggers, the improved sensitivity is due to better trigger acceptance for muons in the forward region. Stau model sensitivity benefits from all of the improvements above and especially from the new LRT triggers since the leptons tend to have lower p_T. All models benefit at high masses from the additional Run 3 data.

Table 2: Expected and observed yields in the signal regions and model-independent upper limits derived using pseudo-experiments. Left to right: background-only model post-fit total expected background, with the combined statistical and systematic uncertainties; observed data; 95% CL upper limits on the visible cross-section ($\langle A\epsilon\sigma\rangle^{95}_{\text{obs}}$) and on the number of signal events (S^{95}_{obs}). The sixth column (S^{95}_{exp}) shows the expected 95% CL upper limit on the number of signal events, given the expected number (and $\pm1\sigma$ excursions of the expectation) of background events. The last two columns indicate the confidence level of the background-only hypothesis (CL_b) and discovery p-value with the corresponding Gaussian significance ($Z(s = 0)$). CL_b provides a measure of compatibility of the observed data with the signal strength hypothesis at the 95% CL limit relative to fluctuations of the background, and $p(s = 0)$ measures compatibility of the observed data with the background-only hypothesis relative to fluctuations of the background. The p-value is capped at 0.5.

| Signal Region	Total Bkg.	Data	$\langle A\epsilon\sigma\rangle^{95}_{\text{obs}}$ [fb]	S^{95}_{obs}	S^{95}_{exp}	CL_b	$p(s = 0)$ (Z)
SRee-high-p_T-Run2	0.031 ± 0.031	0	0.02	3.0	$3.0^{+0.0}_{-0.0}$	0.46	0.5 (0)
SRee-high-p_T-Run3	0.06 ± 0.05	0	0.05	3.0	$3.0^{+0.0}_{-0.1}$	0.45	0.5 (0)
SRee-LRT	$0.0016^{+0.0029}_{-0.0016}$	1	0.07	4.1	$3.1^{+0.0}_{-0.1}$	0.97	0.01 (2.2)
SR$\mu\mu$-high-p_T-Run2	$0.02^{+0.22}_{-0.02}$	0	0.02	3.0	$3.0^{+0.0}_{-0.0}$	0.49	0.5 (0)
SR$\mu\mu$-high-p_T-Run3	$0.01^{+0.11}_{-0.01}$	0	0.05	3.0	$3.0^{+0.0}_{-0.0}$	0.48	0.5 (0)
SR$\mu\mu$-LRT	$0.02^{+0.04}_{-0.02}$	0	0.05	3.0	$3.0^{+0.0}_{-0.0}$	0.49	0.5 (0)
SR$e\mu$-high-p_T-Run2	$0.0016^{+0.0033}_{-0.0016}$	0	0.02	3.0	$3.0^{+0.0}_{-0.1}$	0.50	0.5 (0)
SR$e\mu$-high-p_T-Run3	$0.004^{+0.010}_{-0.004}$	0	0.05	3.0	$3.1^{+0.0}_{-0.0}$	0.50	0.5 (0)
SR$e\mu$-LRT	$0.2^{+0.4}_{-0.2}$	0	0.05	3.0	$3.0^{+0.1}_{-0.1}$	0.45	0.5 (0)
SR-EMBDT	$1.0^{+2.3}_{-0.9}$	3	0.13	7.1	$5.7^{+1.9}_{-0.8}$	0.77	0.2 (0.9)
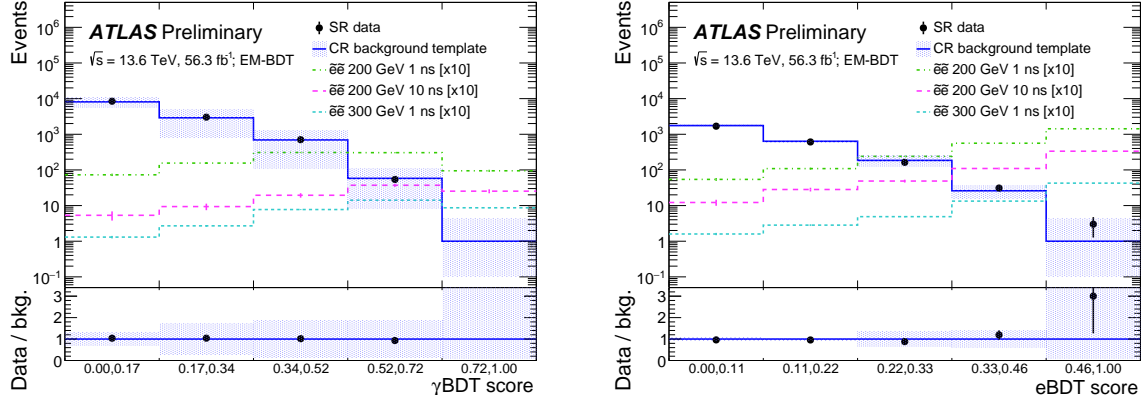
Figure 4: BDT score distributions for the γBDT (left), and eBDT (right) comparing the expected yields from the control region to the observed data. Selectron pair-production models with a mass of 300 GeV and lifetime 10 ns and 200 GeV and 30 ns are overlaid with 10 times the expected yield.
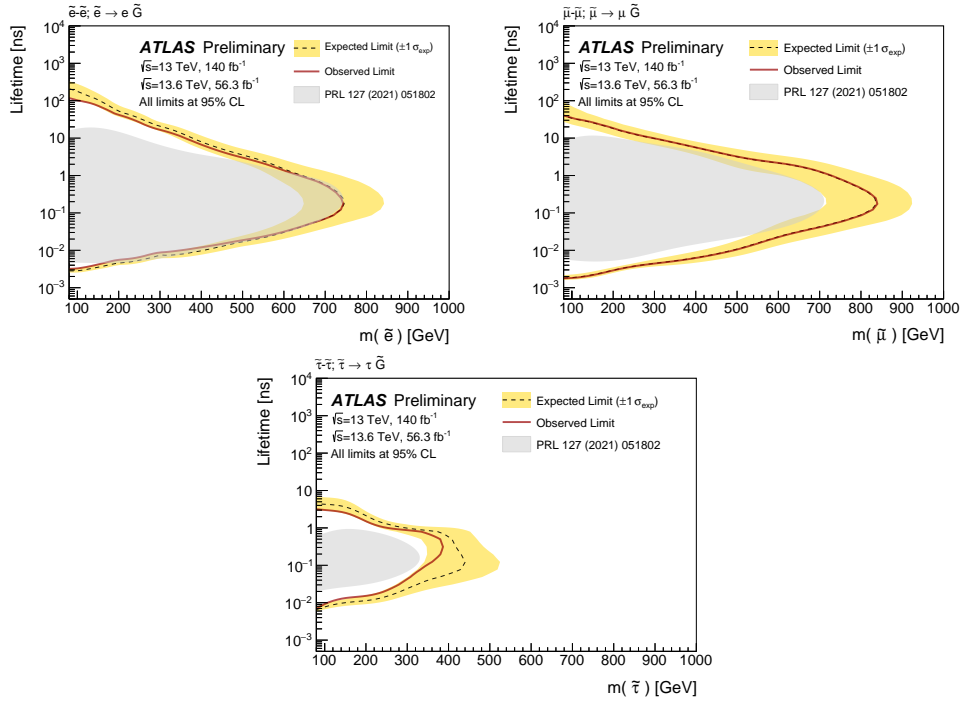

Figure 5: Expected and observed 95% CL exclusion contours for the selectron (left), smuon (right), and stau (bottom) models. The selectron and stau limits are computed using both the ABCD and EM-BDT regions, while the smuon limits are from the ABCD regions only. The dashed line indicates the expected limit and the surrounding band shows the 1σ variation of the expected limit due to uncertainties on the background prediction and experimental uncertainties on the signal modelling. The gray shaded area illustrates the observed exclusion obtained in the prior ATLAS Run 2 analysis [22].

9 Conclusion

A search for BSM physics using 56.3 fb^{-1} of data collected during 2022-2023 with $\sqrt{s}$ = 13.6 TeV, combined with the full Run 2 dataset in some regions, has been presented. The analysis focuses on the signature of displaced electrons and/or muons, consistent with the decay of a long-lived BSM particle. The event selection exploits new Run 3 triggers that employ LRT for sensitivity to lower momentum final state particles. Two orthogonal approaches are used, one focusing on dilepton events and another using LAr measurements and multivariate techniques for expanded sensitivity to single electron and photon-reconstructed events.

The observed event yields in the various signal regions are consistent with the SM background expectations. The results are therefore used to set model-independent limits on the production of displaced electrons and muons. The combined analysis results are interpreted in a benchmark GMSB model with pair-produced long-lived sleptons that decay to the lepton of the same flavor and a nearly massless gravitino, providing exclusion contours which extend significantly beyond previous results. For example, 95% CL exclusions are obtained for 150 GeV selectrons with lifetime values ranging from 4 ps to 70 ns, and selectrons, smuons and staus with 0.3 ns lifetime are excluded up to 740 GeV, 840 GeV, and 380 GeV, respectively.

References

[1] G. R. Farrar and P. Fayet, *Phenomenology of the production, decay, and detection of new hadronic states associated with supersymmetry*, Phys. Lett. B **76** (1978) 575 (cit. on p. 2).

[2] Y. Golfand and E. Likhtman, *Extension of the Algebra of Poincare Group Generators and Violation of P Invariance*, JETP Lett. **13** (1971) 323, [Pisma Zh. Eksp. Teor. Fiz. **13** (1971) 452] (cit. on p. 2).

[3] D. Volkov and V. Akulov, *Is the neutrino a goldstone particle?* Phys. Lett. B **46** (1973) 109 (cit. on p. 2).

[4] J. Wess and B. Zumino, *Supergauge transformations in four dimensions*, Nucl. Phys. B **70** (1974) 39 (cit. on p. 2).

[5] J. Wess and B. Zumino, *Supergauge invariant extension of quantum electrodynamics*, Nucl. Phys. B **78** (1974) 1 (cit. on p. 2).

[6] S. Ferrara and B. Zumino, *Supergauge invariant Yang-Mills theories*, Nucl. Phys. B **79** (1974) 413 (cit. on p. 2).

[7] A. Salam and J. Strathdee, *Super-symmetry and non-Abelian gauges*, Phys. Lett. B **51** (1974) 353 (cit. on p. 2).

[8] R. Barbier et al., *R-Parity-violating supersymmetry*, Phys. Rept. **420** (2005) 1, arXiv: hep-ph/0406039 [hep-ph] (cit. on p. 2).

[9] B. C. Allanach, M. A. Bernhardt, H. K. Dreiner, C. H. Kom, and P. Richardson, *Mass spectrum in R-parity violating minimal supergravity and benchmark points*, Phys. Rev. D **75** (2007) 035002, arXiv: hep-ph/0609263 (cit. on p. 2).

[10] G. Giudice and A. Romanino, *Split supersymmetry*, Nucl. Phys. B **699** (2004) 65, arXiv: hep-ph/0406088 (cit. on p. 2), Erratum: Nucl. Phys. B **706** (2005) 487.

[11] N. Arkani-Hamed and S. Dimopoulos, *Supersymmetric unification without low energy supersymmetry and signatures for fine-tuning at the LHC*, JHEP **06** (2005) 073, arXiv: `hep-th/0405159` (cit. on p. 2).

[12] M. Dine and W. Fischler, *A phenomenological model of particle physics based on supersymmetry*, Phys. Lett. B **110** (1982) 227 (cit. on p. 2).

[13] L. Alvarez-Gaumé, M. Claudson, and M. B. Wise, *Low-energy supersymmetry*, Nucl. Phys. B **207** (1982) 96 (cit. on p. 2).

[14] C. R. Nappi and B. A. Ovrut, *Supersymmetric extension of the SU(3) x SU(2) x U(1) model*, Phys. Lett. B **113** (1982) 175 (cit. on p. 2).

[15] T. Appelquist, H.-C. Cheng, and B. A. Dobrescu, *Bounds on universal extra dimensions*, Phys. Rev. D **64** (2001) 035002, arXiv: `hep-ph/0012100 [hep-ph]` (cit. on p. 2).

[16] H.-C. Cheng, K. T. Matchev, and M. Schmaltz, *Bosonic supersymmetry? Getting fooled at the CERN LHC*, Phys. Rev. D **66** (2002) 056006, arXiv: `hep-ph/0205314 [hep-ph]` (cit. on p. 2).

[17] M. J. Strassler, *Possible effects of a hidden valley on supersymmetric phenomenology*, (2006), arXiv: `hep-ph/0607160` (cit. on p. 2).

[18] J. Alwall, M.-P. Le, M. Lisanti, and J. G. Wacker, *Searching for directly decaying gluinos at the Tevatron*, Phys. Lett. B **666** (2008) 34, arXiv: `0803.0019 [hep-ph]` (cit. on p. 2).

[19] J. Alwall, P. C. Schuster, and N. Toro, *Simplified models for a first characterization of new physics at the LHC*, Phys. Rev. D **79** (2009) 075020, arXiv: `0810.3921 [hep-ph]` (cit. on p. 2).

[20] D. Alves et al., *Simplified models for LHC new physics searches*, J. Phys. G **39** (2012) 105005, arXiv: `1105.2838 [hep-ph]` (cit. on p. 2).

[21] J. A. Evans and J. Shelton, *Long-lived staus and displaced leptons at the LHC*, JHEP **04** (2016) 056, ISSN: 1029-8479, URL: `http://dx.doi.org/10.1007/JHEP04(2016)056` (cit. on p. 2).

[22] ATLAS Collaboration, *Search for Displaced Leptons in $\sqrt{s}$ = 13 TeV pp Collisions with the ATLAS Detector*, Phys. Rev. Lett. **127** (2021) 051802, arXiv: `2011.07812 [hep-ex]` (cit. on pp. 2, 3, 9, 11, 18, 19).

[23] ALEPH Collaboration, *Search for gauge mediated SUSY breaking topologies in e^+e^- collisions at centre-of-mass energies up to 209 GeV*, Eur. Phys. J. C **25** (2002) 339, arXiv: `hep-ex/0203024` (cit. on p. 2).

[24] OPAL Collaboration, *Searches for Gauge-Mediated Supersymmetry Breaking topologies in e^+e^- collisions at centre-of-mass energies up to $\sqrt{s}$ = 209 GeV*, Eur. Phys. J. C **46** (2006) 307, arXiv: `hep-ex/0507048` (cit. on p. 2).

[25] DELPHI Collaboration, *Searches for supersymmetric particles in e^+e^- collisions up to 208 GeV and interpretation of the results within the MSSM*, Eur. Phys. J. C **31** (2003) 421, revised version number 1 submitted on 2003-11-24 16:52:43, URL: `https://cds.cern.ch/record/681867` (cit. on p. 2).

[26] DELPHI Collaboration, *Search for supersymmetric particles in light gravitino scenarios and sleptons NLSP*, Eur. Phys. J. C **27** (2003) 153, arXiv: `hep-ex/0303025` (cit. on p. 2).

[27] ALEPH, DELPHI, L3, OPAL Experiments,
Combined LEP GMSB Stau/Smuon/Selectron Results, 189-208 GeV, LEPSUSYWG/02-09.2, 2002,
URL: http://lepsusy.web.cern.ch/lepsusy/www/gmsb_summer02/lepgmsb.html
(cit. on p. 2).

[28] CMS Collaboration, *Search for long-lived particles decaying to leptons with large impact parameter in proton–proton collisions at $\sqrt{s}$ = 13 TeV*, Eur. Phys. J. C **82** (2022) 153,
arXiv: 2110.04809 [hep-ex] (cit. on p. 2).

[29] ATLAS Collaboration, *Search for pairs of muons with small displacements in pp collisions at $\sqrt{s}$ = 13 TeV with the ATLAS detector*, Phys. Lett. B **846** (2023) 138172,
arXiv: 2305.02005 [hep-ex] (cit. on p. 2).

[30] ATLAS Collaboration,
Performance of the reconstruction of large impact parameter tracks in the inner detector of ATLAS,
Eur. Phys. J. C **83** (2023) 1081, arXiv: 2304.12867 [hep-ex] (cit. on p. 3).

[31] ATLAS Collaboration, *The ATLAS Trigger System for LHC Run 3 and Trigger performance in 2022*,
Journal of Instrumentation **19** (2024) P06029, arXiv: 2401.06630 [hep-ex],
URL: https://dx.doi.org/10.1088/1748-0221/19/06/P06029 (cit. on pp. 3, 5).

[32] ATLAS Collaboration, *Search in diphoton and dielectron final states for displaced production of Higgs or Z bosons with the ATLAS detector in $\sqrt{s}$ = 13 TeV pp collisions*,
Phys. Rev. D **108** (2023) 012012, arXiv: 2304.12885 [hep-ex] (cit. on pp. 3, 6).

[33] ATLAS Collaboration, *Search for displaced photons produced in exotic decays of the Higgs boson using 13 TeV pp collisions with the ATLAS detector*, Phys. Rev. D **108** (2023) 032016,
arXiv: 2209.01029 [hep-ex] (cit. on pp. 3, 6).

[34] ATLAS Collaboration, *The ATLAS Experiment at the CERN Large Hadron Collider*,
JINST **3** (2008) S08003 (cit. on p. 3).

[35] ATLAS Collaboration, *The ATLAS experiment at the CERN Large Hadron Collider: a description of the detector configuration for Run 3*, Journal of Instrumentation **19** (2024) P05063,
URL: https://dx.doi.org/10.1088/1748-0221/19/05/P05063 (cit. on pp. 3, 4).

[36] ATLAS Collaboration, *Performance of the ATLAS trigger system in 2015*,
Eur. Phys. J. C **77** (2017) 317, arXiv: 1611.09661 [hep-ex] (cit. on pp. 4, 6).

[37] ATLAS Collaboration, *The ATLAS Collaboration Software and Firmware*,
ATL-SOFT-PUB-2021-001, 2021, URL: https://cds.cern.ch/record/2767187 (cit. on p. 4).

[38] ATLAS Collaboration, *Software and computing for Run 3 of the ATLAS experiment at the LHC*,
(2024), arXiv: 2404.06335 [hep-ex] (cit. on pp. 4, 6).

[39] ATLAS Collaboration,
Performance of the reconstruction of large impact parameter tracks in the inner detector of ATLAS,
Eur. Phys. J. C **83** (2023) 1081, arXiv: 2304.12867 [hep-ex] (cit. on pp. 5, 16).

[40] ATLAS Collaboration, *ATLAS data quality operations and performance for 2015–2018 data-taking*,
JINST **15** (2020) P04003, arXiv: 1911.04632 [physics.ins-det] (cit. on p. 6).

[41] ATLAS Collaboration,
Luminosity determination in pp collisions at $\sqrt{s}$ = 13 TeV using the ATLAS detector at the LHC,
Eur. Phys. J. C **83** (2023) 982, arXiv: 2212.09379 [hep-ex] (cit. on p. 6).

[42] ATLAS Collaboration,
Preliminary analysis of the luminosity calibration of the ATLAS 13.6 *TeV data recorded in 2022*,
ATL-DAPR-PUB-2023-001, 2023, URL: https://cds.cern.ch/record/2853525 (cit. on p. 6).

[43] ATLAS Collaboration,
Preliminary analysis of the luminosity calibration for the ATLAS 13.6 TeV data recorded in 2023,
ATL-DAPR-PUB-2024-001, 2024, URL: https://cds.cern.ch/record/2900949 (cit. on p. 6).

[44] G. Avoni et al., *The new LUCID-2 detector for luminosity measurement and monitoring in ATLAS*,
JINST **13** (2018) P07017 (cit. on p. 6).

[45] ATLAS Collaboration, *The ATLAS Trigger System for LHC Run 3 and Trigger performance in 2022*,
(2024), arXiv: 2401.06630 [hep-ex] (cit. on pp. 6, 16).

[46] ATLAS Collaboration, *Performance of electron and photon triggers in ATLAS during LHC Run 2*,
Eur. Phys. J. C **80** (2020) 47, arXiv: 1909.00761 [hep-ex] (cit. on p. 6).

[47] ATLAS Collaboration, *Performance of the ATLAS muon triggers in Run 2*,
JINST **15** (2020) P09015, arXiv: 2004.13447 [physics.ins-det] (cit. on p. 6).

[48] ATLAS Collaboration,
The ATLAS inner detector trigger performance in pp collisions at 13 *TeV during LHC Run 2*,
Eur. Phys. J. C **82** (2022) 206, arXiv: 2107.02485 [hep-ex] (cit. on p. 6).

[49] J. Alwall et al., *The automated computation of tree-level and next-to-leading order differential cross sections, and their matching to parton shower simulations*, JHEP **07** (2014) 079,
arXiv: 1405.0301 [hep-ph] (cit. on p. 7).

[50] T. Sjöstrand, S. Mrenna, and P. Skands, *PYTHIA 6.4 physics and manual*, JHEP **05** (2006) 026,
arXiv: hep-ph/0603175 (cit. on p. 7).

[51] ATLAS Collaboration, *ATLAS Pythia 8 tunes to 7 TeV data*, ATL-PHYS-PUB-2014-021, 2014,
URL: https://cds.cern.ch/record/1966419 (cit. on p. 7).

[52] NNPDF Collaboration, R. D. Ball, et al., *Parton distributions with LHC data*,
Nucl. Phys. B **867** (2013) 244, arXiv: 1207.1303 [hep-ph] (cit. on p. 7).

[53] S. Agostinelli et al., *GEANT4–a simulation toolkit*, Nucl. Instrum. Meth. A **506** (2003) 250
(cit. on p. 7).

[54] G. Aad et al., *Emulating the impact of additional proton–proton interactions in the ATLAS simulation by presampling sets of inelastic Monte Carlo events*, Comput. Softw. Big Sci. **6** (2022) 3,
arXiv: 2102.09495 [hep-ex] (cit. on p. 7).

[55] S. Porteboeuf, T. Pierog, and K. Werner,
"Producing Hard Processes Regarding the Complete Event: The EPOS Event Generator,"
45th Rencontres de Moriond on QCD and High Energy Interactions, Gioi Publishers, 2010 135,
arXiv: 1006.2967 [hep-ph] (cit. on p. 7).

[56] T. Pierog, I. Karpenko, J. M. Katzy, E. Yatsenko, and K. Werner, *EPOS LHC: Test of collective hadronization with data measured at the CERN Large Hadron Collider*,
Phys. Rev. C **92** (2015) 034906, arXiv: 1306.0121 [hep-ph] (cit. on p. 7).

[57] *The Pythia 8 A3 tune description of ATLAS minimum bias and inelastic measurements incorporating the Donnachie-Landshoff diffractive model*, (2016) (cit. on p. 7).

[58] W. Beenakker et al., *Production of Charginos, Neutralinos, and Sleptons at Hadron Colliders*,
Phys. Rev. Lett. **83** (1999) 3780, arXiv: `hep-ph/9906298` (cit. on p. 7),
Erratum: Phys. Rev. Lett. **100** (2008) 029901.

[59] J. Debove, B. Fuks, and M. Klasen,
Threshold resummation for gaugino pair production at hadron colliders,
Nucl. Phys. B **842** (2011) 51, arXiv: `1005.2909 [hep-ph]` (cit. on p. 7).

[60] B. Fuks, M. Klasen, D. R. Lamprea, and M. Rothering,
Gaugino production in proton-proton collisions at a center-of-mass energy of 8 *TeV*,
JHEP **10** (2012) 081, arXiv: `1207.2159 [hep-ph]` (cit. on p. 7).

[61] B. Fuks, M. Klasen, D. R. Lamprea, and M. Rothering,
Precision predictions for electroweak superpartner production at hadron colliders with RESUMMINO,
Eur. Phys. J. C **73** (2013) 2480, arXiv: `1304.0790 [hep-ph]` (cit. on p. 7).

[62] J. Fiaschi and M. Klasen, *Neutralino-chargino pair production at NLO+NLL with
resummation-improved parton density functions for LHC Run II*, Phys. Rev. D **98** (2018) 055014,
arXiv: `1805.11322 [hep-ph]` (cit. on p. 7).

[63] J. Fiaschi, B. Fuks, M. Klasen, and A. Neuwirth,
Electroweak superpartner production at 13.6 Tev with Resummino, Eur. Phys. J. C **83** (2023) 707,
arXiv: `2304.11915 [hep-ph]` (cit. on p. 7).

[64] ATLAS Collaboration, *Electron and photon performance measurements with the ATLAS detector
using the 2015–2017 LHC proton-proton collision data*, JINST **14** (2019) P12006,
arXiv: `1908.00005 [hep-ex]` (cit. on pp. 8, 9, 16).

[65] ATLAS Collaboration, *Muon reconstruction and identification efficiency in ATLAS using the full
Run 2 pp collision data set at* $\sqrt{s}$ = 13 *TeV*, Eur. Phys. J. C **81** (2021) 578,
arXiv: `2012.00578 [hep-ex]` (cit. on pp. 8, 9, 16).

[66] ATLAS Collaboration, *Search for long-lived, massive particles in events with a displaced vertex and
a muon with large impact parameter in pp collisions at* $\sqrt{s}$ = 13 *TeV with the ATLAS detector*,
Phys. Rev. D **102** (2020) 032006, arXiv: `2003.11956 [hep-ex]` (cit. on p. 9).

[67] ATLAS Collaboration,
Jet reconstruction and performance using particle flow with the ATLAS Detector,
Eur. Phys. J. C **77** (2017) 466, arXiv: `1703.10485 [hep-ex]` (cit. on p. 9).

[68] M. Cacciari, G. P. Salam, and G. Soyez, *The anti-k_t jet clustering algorithm*, JHEP **04** (2008) 063,
arXiv: `0802.1189 [hep-ph]` (cit. on p. 9).

[69] ATLAS Collaboration, *Performance of pile-up mitigation techniques for jets in pp collisions at*
$\sqrt{s}$ = 8 *TeV using the ATLAS detector*, Eur. Phys. J. C **76** (2016) 581,
arXiv: `1510.03823 [hep-ex]` (cit. on p. 9).

[70] ATLAS Collaboration, *Performance of missing transverse momentum reconstruction with the
ATLAS detector using proton–proton collisions at* $\sqrt{s}$ = 13 *TeV*, Eur. Phys. J. C **78** (2018) 903,
arXiv: `1802.08168 [hep-ex]` (cit. on p. 16).

[71] ATLAS Collaboration, *ATLAS Computing Acknowledgements*, ATL-SOFT-PUB-2023-001, 2023,
URL: `https://cds.cern.ch/record/2869272` (cit. on p. 20).